ACS Catalysis

Research Article

pubs.acs.org/acscatalysis

Methanol to Olefins over H-MCM-22 Zeolite: Theoretical Study on the Catalytic Roles of Various Pores

Sen Wang,[†,‡] Zhihong Wei,[†] Yanyan Chen,[†] Zhangfeng Qin,*[,†] Hong Ma,[†,‡] Mei Dong,[†] Weibin Fan,[†] and Jianguo Wang*[,†]

[†]State Key Laboratory of Coal Conversion, Institute of Coal Chemistry, Chinese Academy of Sciences, P.O. Box 165, Taiyuan, Shanxi 030001, People's Republic of China

[‡]University of Chinese Academy of Sciences, Beijing 100049, People's Republic of China

Supporting Information

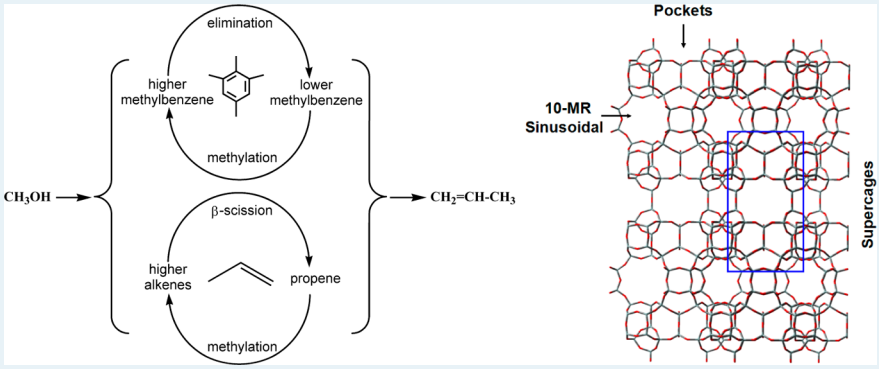

ABSTRACT: H-MCM-22 zeolite bears three types of pores, supercages, sinusoidal channels, and pockets, and exhibits excellent catalytic performance in the process of methanol to olefins (MTO); however, the catalytic role that each type plays in MTO is still unclear. In this work, density functional theory considering dispersive interactions (DFT-D) was used to elucidate the contributions of various pores in H-MCM-22 to MTO. The results demonstrated that these three types of pores are different in their catalytic action on MTO, because of the large differences in pore size and shape that determine the space confinement and electrostatic stabilization effects. The formation of propene is predicted to take place in the supercages, where propene can be effectively produced through both polyMB and alkene cycles, with a relatively low free energy barrier as well as low enthalpy barrier and entropy loss for the rate-determining steps. In the sinusoidal channels, the free energy barrier of the methylation and cracking steps is elevated due to the space confinement and the reactivity of alkenes is also markedly depressed in the narrow channels, in comparison with those in the supercages; as a result, the contribution of the sinusoidal channels to the entire propene formation is minor. Meanwhile, the pockets are probably detrimental to MTO, as certain large intermediates such as 1,1,2,6-tetramethyl-4-isopropylbenzenium cations are easily formed in the pockets but are difficult to decompose due to the lack of an electrostatic stabilization effect from the zeolite framework, which elevates the total free energy barrier and may lead to a rapid deactivation of these active sites. In comparison with the difference in pore size and structure, the difference of various pores in the acid strength of the active sites exhibits an insignificant effect on their catalytic behaviors in MTO. The theoretical insights in this work are conducive to a subsequent investigation on the MTO mechanism and the development of better MTO catalysts and reaction processes.

KEYWORDS: *H-MCM-22, supercages, sinusoidal channels, pockets, methanol-to-olefins, polyMB cycle, alkene cycle, density functional theory*

1. INTRODUCTION

As methanol can be expediently produced via syngas from multifarious carbon resources such as coal, natural gas, and biomass,[1−5] the conversion of methanol to olefins (MTO) over acidic zeolite catalysts has been turning into an increasingly important alternative to naphtha cracking to get light olefins.[6−8] A great deal of effort has been devoted in the past decades to elucidate the reaction mechanism of MTO with both experimental and theoretical approaches.[9−14] Among them, the hydrocarbon pool mechanism proposed by Dahl and Kolboe has received wide recognition,[6−8] which assumes that organic molecules, i.e. the hydrocarbon pool species, trapped in the zeolite pores interplay with the inorganic framework and serve as cocatalysts; the olefin products are eliminated from the hydrocarbon pool. Polymethylbenzenes (polyMBs) are considered as the most important active hydrocarbon pool

Received: August 20, 2014
Revised: January 8, 2015
Published: January 12, 2015

DOI: 10.1021/cs501232r
ACS Catal. 2015, 5, 1131−1144

species.[15,16] Via the polyMB-based cycle, two routes have been proposed for the formation of light olefins: i.e., the side-chain route[17−20] and the paring route.[21,22] By directly pulsing different polyMBs and ^{13}C-methanol onto the large pore H-BEA zeolite, Sassi and co-workers found that the side-chain route was the predominant one to produce olefins.[19] Wang and co-workers also confirmed that the side-chain route for MTO reactions was preferable to the paring route by comparing the kinetics of both routes.[23]

Recently, another possible route for the formation of light olefins based on successive methylation and cracking of C_{3+} alkenes, proposed by Dessau,[24] has received extensive attention. By use of ^{13}C labeling technology, a dual-cycle mechanism that involves both the polyMB cycle and the alkene cycle was proposed for MTO by Svelle and co-workers.[25,26] Meanwhile, a series of theoretical investigations also indicated that the alkene cycle was a viable route to the formation of light olefins.[27,28]

A variety of zeolites have been explored as MTO catalysts, due to their unique pore structure and acidity.[29−32] MCM-22 is considered to be one of the most interesting zeolites, which contains three types of pores: two-dimensional sinusoidal channels with an elliptical ring cross section of 4.1 × 5.1 Å, pockets on the external surface (7.1 Å in diameter and 7.0 Å in height), and cylindrical supercages (7.1 Å in diameter and 18.2 Å in height) that are accessible through 10-membered-ring (4.0 × 5.5 Å) windows, as shown in Figure 1.[33] MCM-22 zeolite has been used as a catalyst for a variety of reactions such as isomerization,[34,35] disproportionation,[36] and alkylation,[37] owing to its peculiar pore systems. Recently, H-MCM-22 zeolite has been applied in the MTO process and exhibits surprising catalytic performance with high selectivity to propene and long lifetime,[38] which should also be related to its unique pore structure. Moreover, as one can speculate, three types of pores in H-MCM-22 may also be rather different in their catalytic action on a reaction because of the large difference in the pore size and shape.

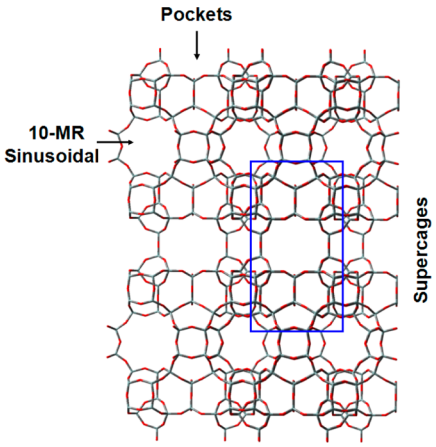

Figure 1. Framework of the H-MCM-22 zeolite with three types of pores: supercages, pockets, and sinusoidal channels.

Although a series of experimental approaches, such as dealumination by acid treatment,[38] silanization,[39] and poisoning by 2,4-dimethylquinoline,[40] have been employed to selectively disclose the catalytic role of each pore system, the observations still remain highly controversial. For examples, Meriaudeau and co-workers suggested that the isomerization occurred mainly in the 10-membered-ring sinusoidal channels;[41] whereas the acid sites located in 12-membered-ring supercages were the primary active centers for the cracking reaction. However, Min and co-workers demonstrated that the formation of propene was dominated by olefin cracking in the 10-membered-ring sinusoidal channels.[38] To elucidate the catalytic role played in MTO by each type of pore in H-MCM-22, the mechanism of methanol conversion in different pores should be considered in detail.

In this work, various pores in H-MCM-22 zeolite, including the sinusoidal channels, supercages, and pockets, were depicted by large cluster models; the catalytic roles of these three types of pores in the MTO process were investigated by density functional theory considering dispersive interactions (DFT-D). The primary mechanism and kinetics for the formation of light olefins over H-MCM-22 were thoroughly considered. The calculations were targeted for the formation of propene as the representative of light olefins, as propene is more expected as the product of MTO in practice than other olefins.

2. COMPUTATIONAL MODELING AND METHODS

45T, 54T, and 36T cluster models were taken from the lattice structure of H-MCM-22 and used to represent the framework of the sinusoidal channels, supercages, and pockets, respectively.[42] For the sinusoidal channels, the 45T cluster model contains two-dimensional 10-membered-ring channels (4.1 × 5.1 Å); the aluminum atom prefers the T3 site when replacing the silicon atom and a charge-balancing proton is produced at O11,[43] as shown in Figure 2a. The 54T cluster model covers 12-membered-ring cylindrical supercages (7.1 × 7.1 × 18.2 Å)

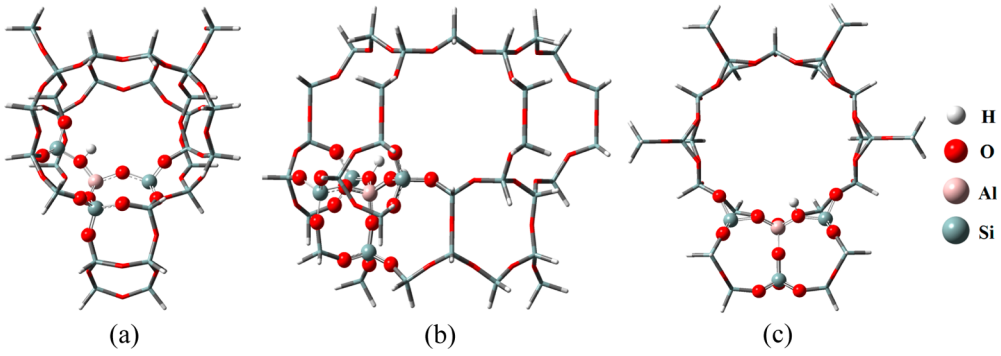

Figure 2. Cluster models used to represent three different types of pores in the H-MCM-22 zeolite: (a) 45T cluster model for the sinusoidal channels; (b) 54T cluster model for the supercages; (c) 36T cluster model for the pockets.

DOI: 10.1021/cs501232r
ACS Catal. 2015, 5, 1131−1144

and 10-membered-ring crossing windows (4.0 × 5.5 Å); a silicon atom is substituted with an aluminum atom at the T4 site and the charge-balancing proton favors bonding with O3 (Figure 2b).[43,44] The pockets (7.1 × 7.1 × 7.0 Å) are represented by the 36T cluster model illustrated in Figure 2c; the aluminum defect is located at the T4 position, and the charge-balancing proton is attached to O3.[43,44] The terminal hydrogen atoms of the cluster models are utilized to saturate the peripheral silicon atom. The distances between the hydrogen atoms and the corresponding silicon atoms are 1.47 Å, and the direction of Si−H bonds is along the pre-existing Si−O bonds.

In addition to the cluster model, the periodic model is also considered as one suitable approach to represent the nanoporous environment of a zeolite. As the entire unit cell is taken into account in the periodic model, it can depict the space confinement and electrostatic stabilization effects of the zeolite framework and is also widely used to investigate the mechanism and kinetics of the MTO process.[45,46] Meanwhile, the crystallographic structure might not be perfectly considered in a small cluster, in contrast to that in a periodic model. However, a large cluster or an extended cluster model such as those used in this work can rationally describe the space confinement and electrostatic stabilization effects of the zeolite framework, provided that it is large enough to account for the distinguishing topological features of a zeolite catalyst.[47−50] Moreover, the cluster approach is able to lower the computational cost, while the localization of transition states and the vibrational analysis are also more straightforward.[49,50]

All density functional theory (DFT) calculations were performed with the Gaussian 09 package.[51] The standard B3LYP functional and the 6-31G(d) basis set were used in all geometry optimizations and frequency calculations of the whole cluster models. The active region of "SiOHAl$(OSi)_2$OSi" and the reacting molecules were allowed to relax while the rest of the zeolite structure was kept fixed at the crystallographic coordinates during the geometry optimizations. Transition states (TS) were guessed by the OPT=TS method and confirmed by the quasi-internal reaction coordinate (quasi-IRC) approach, to verify that each transition state was connected with the corresponding reactants and products. Furthermore, the transition state is a first-order saddle point of the potential energy surface, with only a single imaginary frequency. The obtained reactants and products were verified as being situated in the energy minima points of the potential energy surface, with only real frequencies. To obtain high accurate interaction energies, single-point calculations with the 6-311+G(2df,2p) basis set were refined by the ωB97X-D functional including dispersion interactions, which was a promising method for the main-group thermochemistry, kinetics, and noncovalent interactions.[52,53]

To directly compare the competing elementary reactions within a similar reaction network, it was assumed that in each step all species are adsorbed on the active sites of the zeolites.[54,55] Hence, the intrinsic free energy barrier and unimolecular rate constant are determined. The free energies (ΔG), enthalpies (ΔH), and entropies (ΔS) are obtained from the ωB97X-D/6-311+G(2df, 2p) total electronic energies and the thermal correction from the B3LYP/6-31G(d) frequency calculations by using the partial Hessian vibrational analysis (PHVA) method at 673 K, which includes the atoms that are relaxed during the geometry optimizations. The rate constant (k) at 673 K was calculated by using the classical transition-state theory (TST) from the equation[56]

$$k = \frac{k_B T}{h}\exp(-\Delta G_{int}^{\ddagger}/RT) = \frac{k_B T}{h}\exp(\Delta S_{int}^{\ddagger}/R)\exp(-\Delta H_{int}^{\ddagger}/RT)$$

where k_B is the Boltzmann constant, h is the Planck constant, and $\Delta G_{int}^{\ddagger}$, $\Delta H_{int}^{\ddagger}$, and $\Delta S_{int}^{\ddagger}$ are the changes in the standard molar Gibbs free energy, enthalpy, and entropy at 673 K between the reactants and the transition state (TS), respectively.

To validate the computational modeling and methods described above, the 6-31G(d,p) basis set, including the p orbital for the hydrogen atom, was utilized for the optimization and frequency calculation in a few selected reaction steps; the results for comparison are given in Table S1 and Figure S4b,d,g,h (Supporting Information). It can be found that the differences between the 6-31G(d,p) basis set and the 6-31G(d) basis set are negligible in the calculated energies and structures of the reacting species. As a result, in the subsequent sections, only the results from the ωB97X-D/6-311+G(2df,2p)//B3LYP/6-31G(d) approaches are reported.

To analyze and visualize the noncovalent interactions in zeolite systems, the isosurface plots of the reduced density gradient (RDG) for the transition states of the rate-determining steps of polyMB and alkene cycles in the pockets, supercages, and sinusoidal channels were obtained by calculating the RDG functions and quantity sign $(\lambda_2)\rho$ with the Multiwfn software.[57]

The proton affinity (PA) is obtained as the energy difference between the protonated zeolite and the deprotonated one, i.e. $PA = E_{(Z^-)} - E_{(HZ)}$. The ammonia adsorption energy (ΔE_{ads}) in the active sites is calculated by the equation $\Delta E_{ads} = E_{NH3\text{-}HZ} - (E_{HZ} + E_{NH3})$, where $E_{NH3\text{-}HZ}$ is the total energy of the zeolite system after the adsorption of ammonia, E_{HZ} is the energy of the zeolite system before the adsorption and E_{NH3} is the energy of isolated ammonia.

3. RESULTS AND DISCUSSION

As illustrated in Figure 3, propene may be produced through the polyMB cycle and/or the alkene cycle in the MTO process. Because the polyMB cycle is a space-demanding process, for MTO over H-MCM-22, this cycle is only considered in the pockets and supercages with large pore size, whereas it is unlikely to occur in the sinusoidal channels with a small pore size (4.1 × 5.1 Å), similar to the situation over H-ZSM-22 zeolite (TON, 4.6 × 5.7 Å).[58,59] According to the GC-MS analysis by Min and co-workers,[38] tetramethylbenzene served as the active cocatalyst for the polyMB cycle following the side-chain route. For the alkene cycle, propene is produced through the β scission of higher carbenium ions that are formed by successive methylation steps. Both the C_6^+ and C_7^+ ions may serve as the precursors for cracking in the pockets and supercages, whereas only C_6^+ ion is considered in the sinusoidal channels, due to the restriction of the C_7^+ ion formation by the narrow space. 4-Methyl-2-pentylcarbenium cation and 2,4-dimethyl-2-pentylcarbenium cation are utilized as the representatives of the C_6^+ and C_7^+ ions, respectively, as the hexene cracking is dominated by the secondary to secondary scission, whereas the heptene cracking is dominated by the secondary to tertiary or tertiary to secondary scission.[60]

DOI: 10.1021/cs501232r
ACS Catal. 2015, 5, 1131−1144

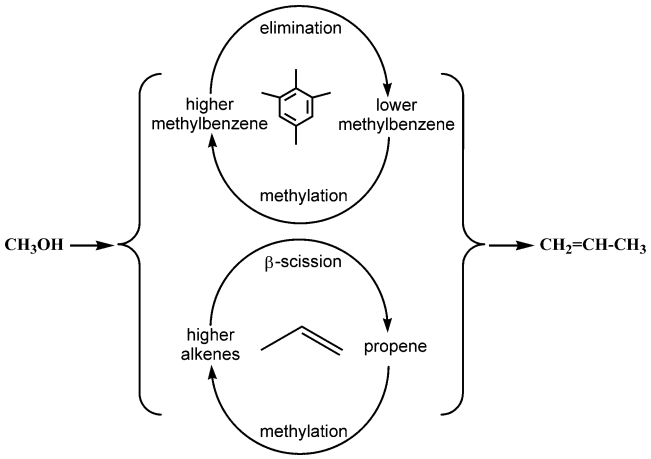

Figure 3. PolyMB cycle (top) and alkene cycle (bottom) proposed for MTO over the H-MCM-22 zeolite used to unravel the catalytic roles of the supercages, pockets, and sinusoidal channels. Via the polyMB cycle, polymethylbenzenes act as the active hydrocarbon pool species, whereas via the alkene cycle, alkenes are the active hydrocarbon pool species.

3.1. MTO in the Pockets. *3.1.1. PolyMB Cycle.* The detailed reaction pathway of MTO via the polyMB cycle is summarized in Figure 4, which assumes that methanol and

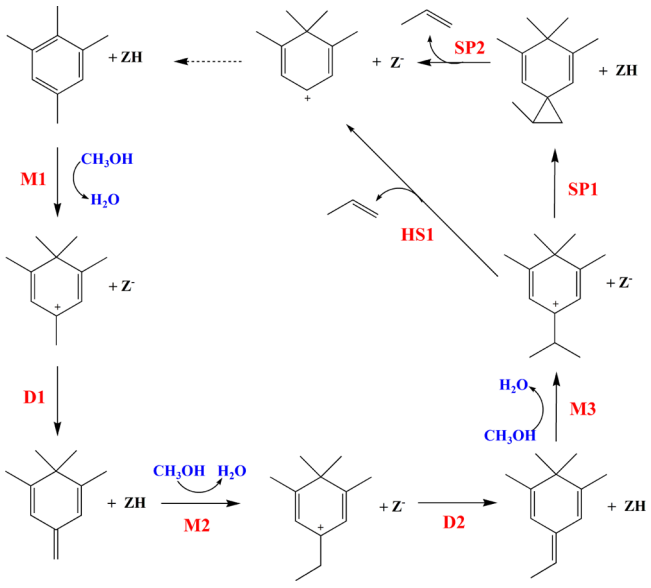

Figure 4. Detailed polyMB cycle for MTO over the H-MCM-22 zeolite, where 1,2,4,6-tetramethylbenzene is considered as the active cocatalyst. For the deprotonation steps (D1 and D2) and olefin elimination steps via the spiro route (SP1 and SP2), a water molecule serves as a proton transfer reagent.

tetramethylbenzene (TMB) molecules have been previously adsorbed in the zeolite pores. The whole cycle then starts from the *gem*-methylation of 1,2,4,6-tetramethylbenzene with methanol (M1), forming a 1,1,2,4,6-pentamethylbenzenium cation, which loses one proton in its side-chain methyl group to give tetramethylmethylenecyclohexadiene containing an exocyclic double bond (D1). The second methanol molecule attacks the exocyclic double bond to give the 1,1,2,6-tetramethyl-4-ethylbenzenium cation (M2), which is then deprotonated to form tetramethylethylenecyclohexadiene (D2). After that, 1,1,2,6-tetramethyl-4-isopropylbenzenium cation is formed through the methylation of tetramethylethylenecyclohexadiene (M3). Finally, propene is produced through two different elimination routes, i.e. the internal hydrogen-shift route (HS1) and the spiro route (SP1 + SP2), which are considered as the main pathways of olefin elimination in MTO.[11,61,62] In the internal hydrogen-shift route (HS1), one ending hydrogen atom of the side-chain alkyl group has to be shifted directly to the ring carbon and meanwhile the C−C bond breaks between the ring carbon and side-chain carbon. In the spiro route, the ending hydrogen atom is first taken off by the active oxygen atom of water to form a spiro intermediate (SP1), which is subsequently attacked by a proton from water; after that, the C−C bond between the ring carbon and side-chain carbon is then broken to eliminate olefin (SP2).

It should be noted that the water molecule formed in the methylation steps is considered as being adsorbed in the zeolite and serves as a coreactant for the deprotonation steps (D1 and D2) and olefin elimination via the spiro route (SP1 and SP2) to facilitate the proton transfer between the intermediates and zeolite framework; however, the water molecule is released as a gaseous species before the olefin elimination via the internal hydrogen-shift route (HS1), because this reaction step has dispensed with the assistance of water. As a result, HS1 and SP1 are different in the intermediate reactant species; HS1 involves only the framework of the pockets or the supercages and the adsorbed 1,1,2,6-tetramethyl-4-isopropylbenzenium cation, whereas the adsorbed water molecule is also implicated in SP1.

The calculated free energy profile of MTO over H-MCM-22 via the polyMB cycle in the pockets is depicted in Figure 5,

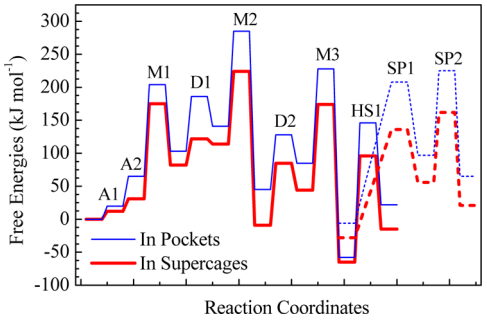

Figure 5. Free energy profiles of the polyMB cycle for MTO over the H-MCM-22 zeolite at 673 K in the supercages and pockets. The framework of various pores and the methanol and 1,2,4,6-tetramethylbenzene molecules in the gaseous phase are taken as the reference state. A1 is the adsorption of methanol, and A2 is the subsequent adsorption of 1,2,4,6-tetramethylbenzene. After M3, propene elimination is separated into two pathways of SP1 + SP2 (adsorbed water assistance) and HS1 (without water assistance).

while the detailed free energy barriers and the relative rate constants at 673 K for all steps are given in Table 1. The separate contributions of the van der Waals interactions to the total free energy barriers can be found in Tables S2−S4 (Supporting Information). The framework of the pockets as well as the methanol and 1,2,4,6-tetramethylbenzene molecules in gaseous phase are taken as the reference state, whereas all the given energies are relative to this state. The calculated adsorption free energies of methanol and 1,2,4,6-tetramethylbenzene are 20 and 45 kJ mol^{-1}, respectively. Three methylation steps of M1−M3 need to overcome free energy barriers of 139, 144, and 143 kJ mol^{-1}, with rate constants of

DOI: 10.1021/cs501232r
ACS Catal. 2015, 5, 1131−1144

Table 1. Calculated Free Energy Barriers ($\Delta G_{int}^{\ddagger}$) and Relative Rate Constants (k) at 673 K of Each Reaction Step for MTO over H-MCM-22 via the PolyMB Cycle and the Alkene Cycle in the Supercages, Pockets, and Sinusoidal Channels

	$\Delta G_{int}^{\ddagger}$ (kJ mol^{-1})			k (s^{-1})		
reaction step	supercage	pocket[a]	sinusoidal channel	supercage	pocket[a]	sinusoidal channel
			PolyMB Cycle			
M1	144	139 (138)		8.98×10^{1}	2.50×10^{2} (2.43×10^{2})	
M2	111	144		3.59×10^{4}	8.72×10^{1}	
M3	130	143		1.06×10^{3}	1.14×10^{2}	
D1	40	82		1.13×10^{10}	5.96×10^{6}	
D2	94	83		6.99×10^{5}	5.31×10^{6}	
SP1	163	214		$3.13 \times 10^{\circ}$	3.60×10^{-4}	
SP2	106	128		8.57×10^{4}	1.58×10^{3}	
HS1	162	204 (197)		$3.74 \times 10^{\circ}$	2.14×10^{-3} (7.33×10^{-3})	
			Alkene Cycle: (a) C_6^+ Route			
M1	150	136	180	3.25×10^{1}	4.04×10^{2}	2.44×10^{-1}
M2(a)	131	149	163	9.44×10^{2}	3.53×10^{1}	$3.04 \times 10^{\circ}$
M3(a)	138	137	175	2.62×10^{2}	3.33×10^{2}	3.45×10^{-1}
D1(a)	44	68	51	5.34×10^{9}	6.82×10^{7}	1.65×10^{9}
D2(a)	32	30	79	4.80×10^{10}	7.16×10^{10}	1.06×10^{7}
E1(a)	94	111	177	6.93×10^{5}	3.13×10^{4}	2.71×10^{-1}
			Alkene Cycle: (b) C_7^+ Route			
M1	150	136		3.25×10^{1}	4.04×10^{2}	
M2(b)	146	129		6.02×10^{1}	1.28×10^{3}	
M3(b)	134	133		5.55×10^{2}	6.85×10^{2}	
M4(b)	141	143		1.69×10^{2}	1.07×10^{2}	
D1(b)	45	79		4.75×10^{9}	1.12×10^{7}	
D2(b)	37	68		1.81×10^{10}	7.21×10^{7}	
D3(b)	9	41		2.95×10^{12}	9.15×10^{9}	
E1(b)	88	65		1.91×10^{6}	1.22×10^{8}	

[a]The values in parentheses are obtained with a larger cluster model of 57T for the pockets.

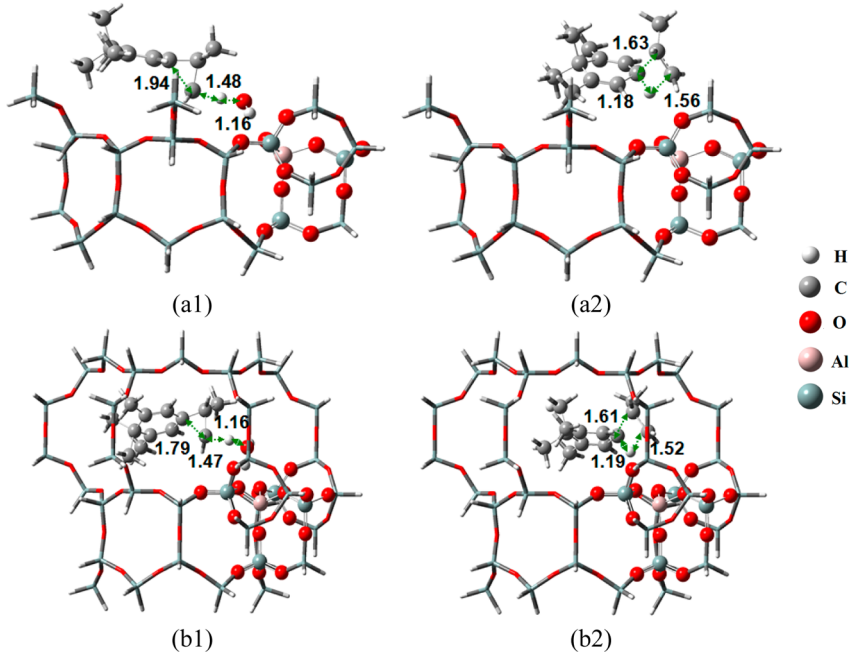

Figure 6. Optimized transition states of the rate-determining steps in the polyMB cycle over the H-MCM-22 zeolite in the pockets (a) and supercages (b): (a1, b1) formation of the spiro intermediate (SP1); (a2, b2) internal hydrogen shift (HS1). The unit of bond distances is Å. The imaginary frequencies of a1, a2, b1, and b2 are −858, −389, −895, and −468 cm^{-1}, respectively.

2.50×10^{2}, 8.72×10^{1}, and 1.14×10^{2} s^{-1}, respectively. Such results are similar to those obtained from the periodic DFT calculations by using the CHA models,[63] indicating that methylation takes place easily without exceptional space confinement. The two deprotonation steps of D1 and D2 are both very fast, with a free energy barrier below 85 kJ mol^{-1}. The elimination of propene through the internal hydrogen-shift (HS1) route has a free energy barrier of 204 kJ mol^{-1} and a rate

DOI: 10.1021/cs501232r
ACS Catal. 2015, 5, 1131−1144

Table 2. Calculated Enthalpy Barriers ($\Delta H_{int}^{\ddagger}$) and Entropy Losses ($-T\Delta S_{int}^{\ddagger}$) at 673 K of Each Reaction Step for MTO over H-MCM-22 via the PolyMB Cycle and the Alkene Cycle in the Supercages, Pockets, and Sinusoidal Channels

	$\Delta H_{int}^{\ddagger}$ (kJ mol^{-1})			$-T\Delta S_{int}^{\ddagger}$ (kJ mol^{-1})		
reaction step	supercage	pocket	sinusoidal channel	supercage	pocket	sinusoidal channel
			PolyMB Cycle			
M1	130	116		14	23	
M2	103	124		8	20	
M3	107	124		23	19	
D1	11	43		29	39	
D2	67	55		27	28	
SP1	133	200		30	14	
SP2	115	125		−9	3	
HS1	141	187		21	17	
			Alkene Cycle: (a) C_6^+ Route			
M1	128	110	136	22	26	44
M2(a)	116	124	121	15	25	42
M3(a)	116	110	136	22	27	39
D1(a)	54	77	65	−10	−9	−14
D2(a)	42	47	84	−10	−17	−5
E1(a)	140	160	203	−46	−49	−26
			Alkene Cycle: (b) C_7^+ Route			
M1	128	110		22	26	
M2(b)	129	114		17	15	
M3(b)	113	104		21	29	
M4(b)	110	119		31	24	
D1(b)	56	82		−11	−3	
D2(b)	48	77		−11	−9	
D3(b)	22	49		−13	−8	
E1(b)	104	106		−16	−41	

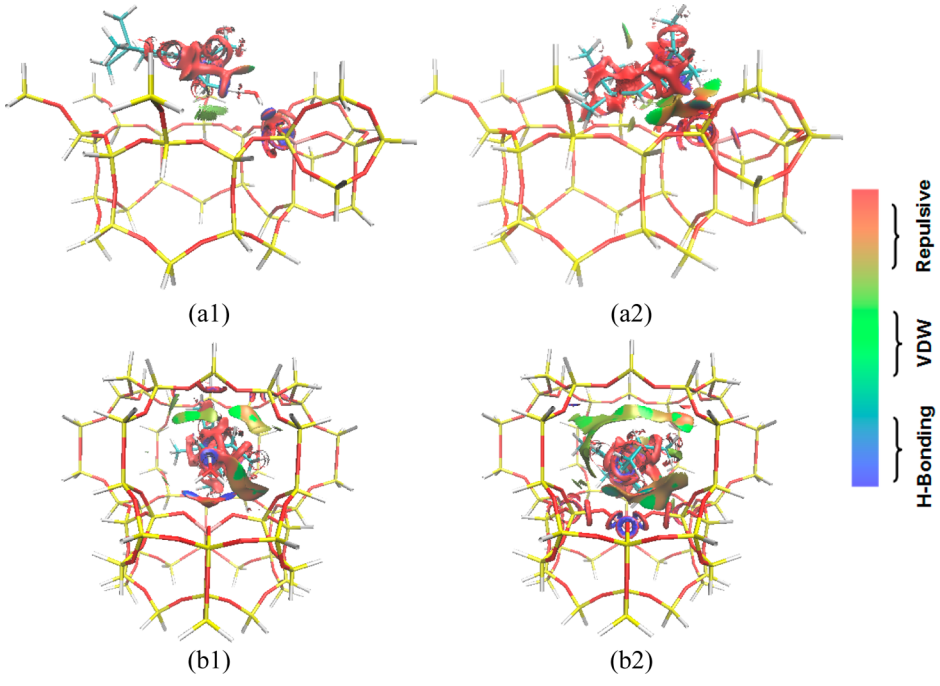

Figure 7. Isosurface plots of the reduced density gradient (s = 0.500 au) for the transition states of the rate-determining step in the polyMB cycle over the H-MCM-22 zeolite in the pockets (a) and supercages (b): (a1, b1) formation of the spiro intermediate (SP1); (a2, b2) internal hydrogen shift (HS1). The isosurfaces of the reduced density gradient are colored according to the values of the quantity sign $(\lambda_2)\rho$ with the indicated RGB scale. VDW represents the van der Waals interactions.

constant of 2.14×10^{-3} s^{-1}, whereas through the spiro route, the formation of a spiro intermediate (SP1) and the breakage of the C−C bond (SP2) require free energy barriers of 214 and 128 kJ mol^{-1}, with rate constants of 3.60×10^{-4} and 1.58×10^{3} s^{-1}, respectively. These results suggest that the elimination of propene is the rate-determining step for the MTO via the polyMB cycle in the pockets. The optimized transition states

DOI: 10.1021/cs501232r
ACS Catal. 2015, 5, 1131−1144

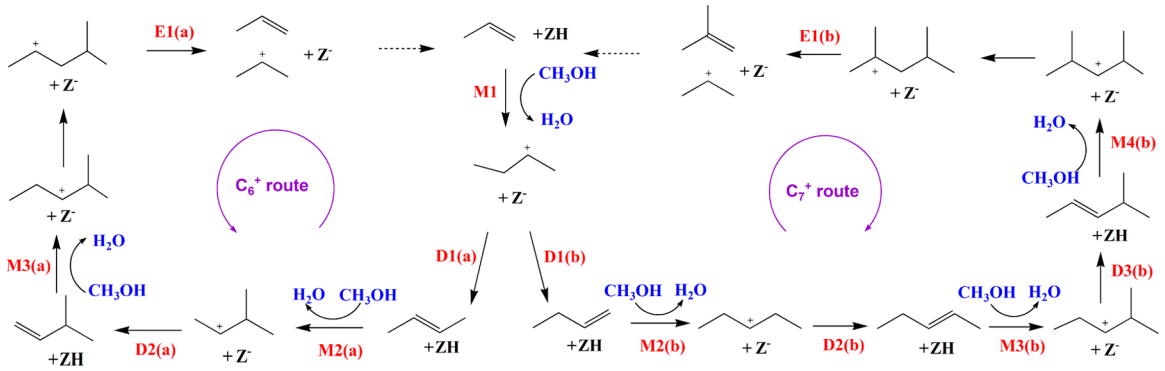

Figure 8. Detailed alkene cycle for MTO over the H-MCM-22 zeolite. According to the alkene precursors designed for cracking, the alkene cycle is divided into the C_6^+ route and C_7^+ route. For the deprotonation steps (D1−D3), the water molecule serves as a proton transfer reagent.

for the polyMB cycle in the pockets are presented in Figure 6a1,a2 and in Figure S1a−f (Supporting Information).

To get further insight into the reaction kinetics and mechanism, the enthalpy barriers ($\Delta H_{int}^{\ddagger}$) and entropy losses ($-T\Delta S_{int}^{\ddagger}$) at 673 K have also been acquired, as summarized in Table 2. The rate-determining steps of HS1 and SP1 show the highest enthalpy barriers, whereas they are similar to the methylation steps in the entropy losses. This suggests that the quite high free energy barriers of olefin elimination in the pockets are mainly contributed by the enthalpy barriers, owing to the inefficient stabilization of the reaction intermediates by the zeolite framework.[49] Meanwhile, as shown in Figure 6a1,a2, the transition states of SP1 and HS1 are exposed to the gaseous phase and become less stabilized due to the lack of strong electrostatic stabilization from the zeolite framework,[64] which results in a high enthalpy barrier and, subsequently, a quite high free energy barrier and a very low rate constant for the propene elimination steps. The rate-determining steps of the polyMB cycle have been further studied by visualizing the isosurfaces of the reduced density gradient in real space.[65,66] As shown in Figure 7a1,a2, the isosurfaces of the transition states of HS1 and SP1 exhibit a large red region and a very small green region, confirming that these two steps have a quite high enthalpy barrier due to the lack of electrostatic stabilization on the transition states from the zeolite framework.

The above observations are in line with the conclusions of Van der Mynsbrugge and co-workers;[49] by comparing the influence of zeolite topology on the kinetics of methylation over H-ZSM-5 (MFI) with that over H-ZSM-58 (DDR), they found that the electrostatic stabilization effect of the zeolite framework on the intermediate was crucial to stabilize the intermediate structure. Moreover, Zheng and co-workers investigated the propene hydrogenation over H-ZSM-5 zeolite and also found that the carbenium ion intermediates/transition states can be effectively stabilized through the electrostatic effects induced by the zeolite framework.[67]

To check the validity of the model systems used in this work, as an example, a larger pocket model of 57T was used for the calculation of the first methylation (M1) and internal hydrogen-shift (HS1) steps in comparison with the 36T model for the pockets, as also given in Table 1. For these two steps of M1 and HS1, two models of 57T and 36T only display a very small difference in the free energy barriers (1−7 kJ mol^{-1}) and the rate constants obtained from these two models are also quite close, indicating that current model systems are reasonable to depict the MTO reactions over H-MCM-22.

For the formation of propene via the polyMB cycle in the pockets, all of the free energy barriers of the methylation steps are below 145 kJ mol^{-1}, meaning that the repeated methylation of polyMBs takes place easily, resulting in the rapid growth of the polyMB molecules. However, both the internal hydrogen-shift route and the spiro route are very slow and need a much higher free energy barrier of about 210 kJ mol^{-1}, which may inhibit the release of propene molecules for MTO from the pockets of H-MCM-22 through the polyMB cycle.

3.1.2. Alkene Cycle. The proposed alkene cycle for MTO is presented in Figure 8; similar to the polyMB cycle, it is assumed that methanol and propene molecules have been previously adsorbed in the zeolite pores. Higher carbenium ions, i.e. 2-methyl-3-pentyl carbenium ion and 2,4-dimethyl-3-pentyl carbenium ion, are then formed from the propene molecule through repeated methylations with methanol (M1−M4). The higher carbenium ions may undergo fast intramolecular hydride shifts, forming 2-methyl-4-pentyl carbenium ion and 2,4-dimethyl-2-pentyl carbenium ion. There are various pathways for the intramolecular hydride shifts, and their behavior was also related to special zeolites.[27,28] However, the intramolecular hydride shifts should not be the dominant obstacle in the alkene cycle, as the free energy barriers of the intramolecular hydride shifts are lower than those of the methylation and cracking steps (Table S5 in the Supporting Information). Subsequently, these carbenium ions regenerate lower olefins through β scission (E1).[68−70] Depending on the precursors for cracking, the alkene cycle can be divided into the C_6^+ route (a) and C_7^+ route (b). For each deprotonation step, the water molecule generated from the previous methylation here is also considered as being adsorbed in the zeolite and serves as a coreactant, whereas for the cracking steps the water generated from the last methylation is taken as a gaseous molecule and is not implicated in the cracking steps, as the cracking reactions have dispensed with the assistance of water.

The calculated free energy profiles of the C_6^+ route and C_7^+ route in the pockets are shown in Figures 9 and 10, respectively; the free energy barriers and relative rate constants of each step in the alkene cycle are also given in Table 1. Similarly, the framework of the pockets and the methanol and propene molecules in the gaseous phase are taken as the reference state to get the energies of other species. The calculated adsorption free energies of methanol and propene are 20 and 57 kJ mol^{-1}, respectively. The optimized transition states for the alkene cycle in the pockets are presented in Figure 11a,b as well as in Figures S2a−e and S3a−f in the Supporting Information.

DOI: 10.1021/cs501232r
ACS Catal. 2015, 5, 1131−1144

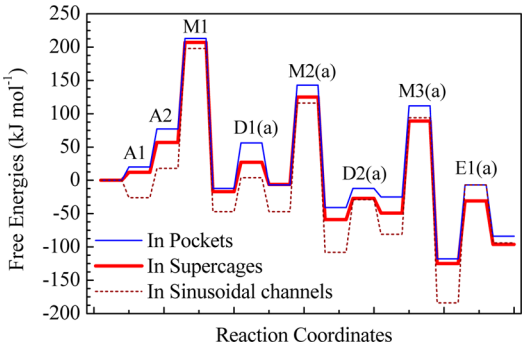

Figure 9. Free energy profiles of the alkene cycle of the C_6^+ route for MTO over the H-MCM-22 zeolite at 673 K in the supercages, pockets, and sinusoidal channels. The framework of various pores and the methanol and propene molecules in the gaseous phase are taken as the reference state. A1 is the adsorption of methanol, and A2 is the subsequent adsorption of propene.

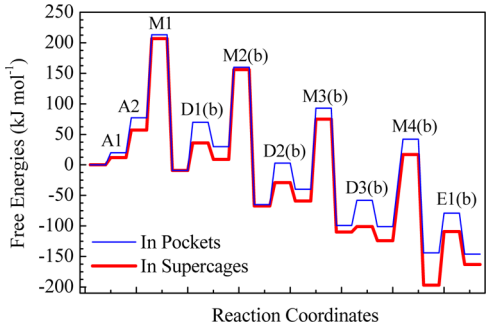

Figure 10. Free energy profiles of the alkene cycle of the C_7^+ route for MTO over the H-MCM-22 zeolite at 673 K in the supercages and pockets. The framework of various pores and the methanol and propene molecules in the gaseous phase are taken as the reference state. A1 is the adsorption of methanol, and A2 is the subsequent adsorption of propene.

Via the C_6^+ route, the methylation steps of M1, M2(a), and M3(a) have free energy barriers of 136, 149, and 137 kJ mol^{-1}, with rate constants of 4.04 × 10^2, 3.53 × 10^1, and 3.33 × 10^2 s^{-1}, respectively. The deprotonation steps of D1(a) and D2(a) take place easily, as they only need a free energy barrier below 70 kJ mol^{-1}. The propene molecule is formed through the cracking of the C_6^+ ion; the free energy barrier and rate constant for this step are 111 kJ mol^{-1} and 3.13 × 10^4 s^{-1}, respectively.

Via the C_7^+ route, the methylation steps of M1, M2(b), M3(b), and M4(b) need to overcome free energy barriers of 136, 129, 133, and 143 kJ mol^{-1}, with rate constants of 4.04 × 10^2, 1.28 × 10^3, 6.85 × 10^2, and 1.07 × 10^2 s^{-1}, respectively. The deprotonation steps of D1(b), D2(b), and D3(b) are fast, as they need a free energy barrier lower than 80 kJ mol^{-1}. The cracking of the C_7^+ ion generates a propoxy group, which will be rapidly deprotonated to produce propene; the cracking step requires a free energy barrier of 65 kJ mol^{-1} with a rate constant of 1.22 × 10^8 s^{-1}.

The highest free energy barriers observed for MTO via the C_6^+ route and C_7^+ route of the alkene cycle in the pockets are 149 and 143 kJ mol^{-1} for the steps of M2(a) and M4(b), respectively, which are significantly lower than those for the propene elimination steps via the polyMB cycle. As given in Table 2, M2(a) and M4(b) of the alkene cycle are similar to HS1 and SP1 of the polyMB cycle in the entropy losses, whereas the enthalpy barriers for the first two steps are about 60−80 kJ mol^{-1} lower than the last two steps, indicating that the relatively low free energy barriers for M2(a) and M4(b) steps are mainly ascribed to their low enthalpy barriers.

As illustrated in Figure 11a,b, the transition states for M2(a) and M4(b) have a relatively small size and are wrapped in the internals of the pockets. As the transition states here are stabilized by the zeolite framework, the enthalpy barriers and the total free energy barriers of the rate-determining steps in

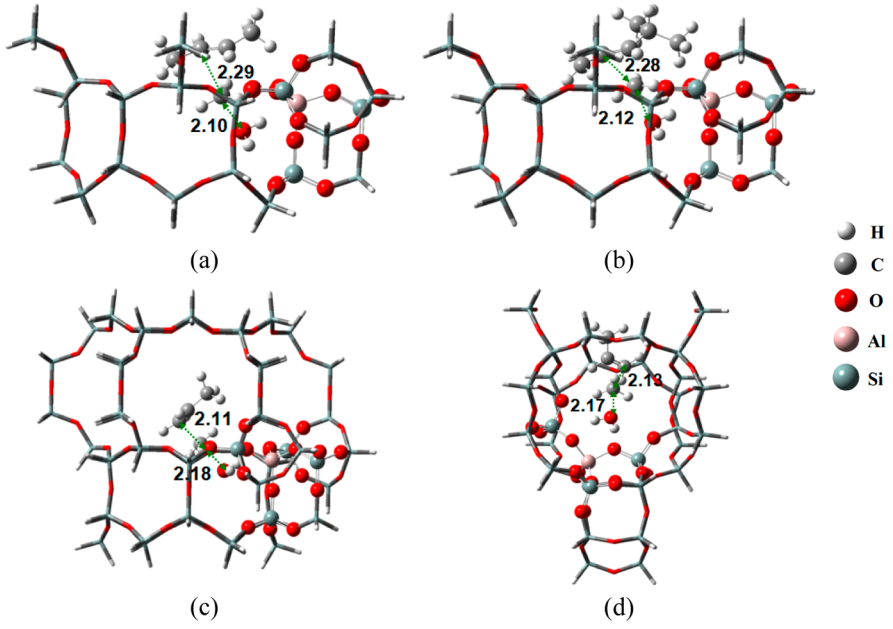

Figure 11. Optimized transition states of the rate-determining steps in the alkene cycle for MTO over the H-MCM-22 zeolite: (a) for the methylation (M2(a)) in the pockets; (b) for the methylation (M4(b)) in the pockets; (c) for the methylation (M1) in the supercages; (d) for the methylation (M1) in the sinusoidal channels. The unit of bond distances is Å. The imaginary frequencies of a−d are −351, −354, −359, and −363 cm^{-1}, respectively.

DOI: 10.1021/cs501232r
ACS Catal. 2015, 5, 1131−1144

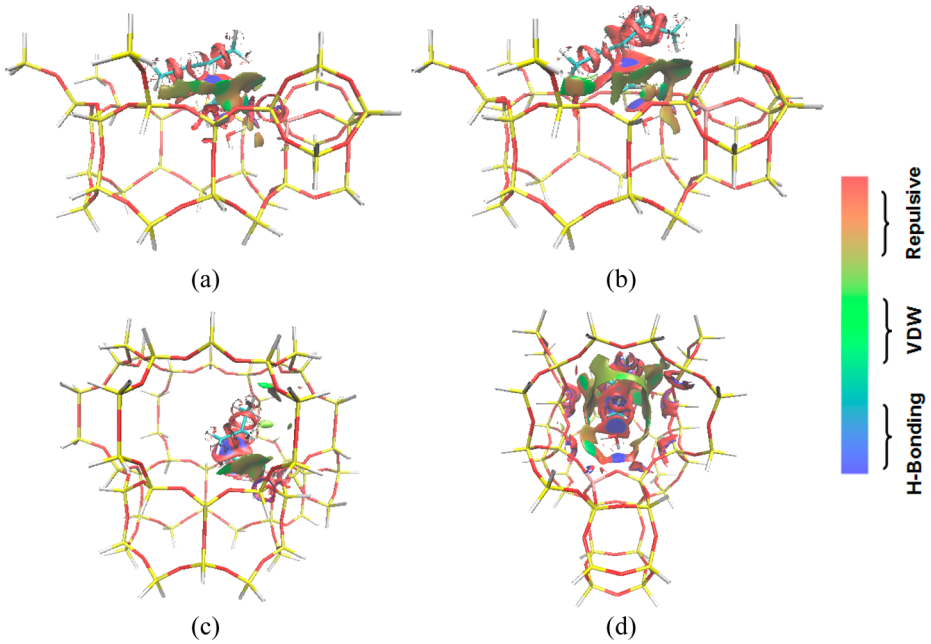

Figure 12. Isosurface plots of the reduced density gradient (s = 0.500 au) for the transition states of the rate-determining step in the alkene cycle over the H-MCM-22 zeolite: (a) for the methylation (M2(a)) in the pockets; (b) for the methylation (M4(b)) in the pockets; (c) for the methylation (M1) in the supercages; and (d) for the methylation (M1) in the sinusoidal channels. The isosurfaces of the reduced density gradient are colored according to the values of the quantity sign $(\lambda_2)\rho$ with the indicated RGB scale. VDW represents the van der Waals interactions.

the alkene cycle can then be reduced. These observations are also supported by the isosurface plots of the reduced density gradient, as shown in Figure 12a,b; in comparison with the transition states of HS1 and SP1 in the polyMB cycle, the transition states of M2(a) and M4(b) in the alkene cycle exhibit an obvious increase of the green regions in the isosurface.

As both the methylation and cracking steps involved in the alkene cycle are feasible in the pockets of H-MCM-22, propene here is likely generated through the alkene cycle. However, it should be noted that the decomposition of 1,1,2,6-tetramethyl-4-isopropylbenzenium cation formed via the polyMB cycle is very slow and is quite difficult due to the low rate constant and high free energy barrier for the olefin elimination reactions, though it can be easily generated through the repeated methylations. Thus, the 1,1,2,6-tetramethyl-4-isopropylbenzenium cation formed in the preceding steps may cover the active sites and even turn into coke, leading to the deactivation of the pockets. The experimental observations also suggested that the pockets show a fast deactivation during the catalytic reactions due to the rapid coke deposition.[38]

3.2. MTO in the Supercages. *3.2.1. PolyMB Cycle.* The polyMB cycle for MTO over H-MCM-22 in the supercages is in nature the same as that in the pockets (Figure 4). The calculated free energy profile of the polyMB cycle in the supercages is also depicted in Figure 5, and the detailed free energy barriers and relative rate constants at 673 K for all steps are given in Table 1. Similar with the elucidation in the pockets, the framework of the supercages as well as the methanol and 1,2,4,6-tetramethylbenzene molecules in the gaseous phase are taken as the reference state to calculate the energies of other species. The calculated adsorption free energies of methanol and 1,2,4,6-tetramethylbenzene are 12 and 19 kJ mol^{-1}, respectively. The optimized transition states of the spiro intermediate formation (SP1) and internal hydrogen-shift (HS1) steps are presented in Figure 6b1,b2, while other optimized transition states are shown in Figure S4a–h in the Supporting Information.

As given in Table 1, three methylation steps of M1–M3 for the polyMB cycle in the supercages require free energy barriers of 144, 111, and 130 kJ mol^{-1}, with rate constants of 8.98 × 10^{1}, 3.59 × 10^{4}, and 1.06 × 10^{3} s^{-1}, respectively. The deprotonation steps (D1 and D2) are also very facile with a free energy barrier below 95 kJ mol^{-1}. In contrast to that in the pockets, the propene elimination in the supercages by the internal hydrogen-shift route (HS1) needs to overcome a free energy barrier of 162 kJ mol^{-1} with a rate constant of 3.74 × 10^{0} s^{-1}, whereas the formation of the spiro intermediate (SP1) and the breakage of the C–C bond (SP2) in the spiro route need to step over energy barriers of 163 and 106 kJ mol^{-1}, with rate constants of 3.13 × 10^{0} and 8.57 × 10^{4} s^{-1}, respectively. Evidently, the elimination of propene is also the rate-determining step for the polyMB cycle in the supercages. However, the free energy barriers for propene elimination in the supercages are about 40 kJ mol^{-1} lower than those in the pockets and the rate constants are about 3 orders higher than those in the pockets, indicating that the propene elimination step here is conquerable and propene can be effectively generated by following the polyMB cycle in the supercages.

The detailed enthalpy barriers ($\Delta H_{int}^{\ddagger}$) and entropy losses ($-T\Delta S_{int}^{\ddagger}$) via the polyMB cycle in the supercages are summarized in Table 2. The enthalpy barriers of HS1 and SP1 in the supercages (141 and 133 kJ mol^{-1}, respectively) are much lower than those in the pockets (187 and 200 kJ mol^{-1}, respectively), whereas the entropy losses in the two pores are nearly the same. Figure 6b1,b2 further illustrates that the transition states of HS1 and SP1 are wrapped inside the cage and are electrostatically stabilized by the zeolite framework, which can effectively reduce the enthalpy barriers of the propene elimination steps and finally depress the total free energy barriers. In the isosurface plots of the reduced density gradient (Figure 7b1,b2), HS1 and SP1 in the supercages have

DOI: 10.1021/cs501232r
ACS Catal. 2015, 5, 1131–1144

a much larger green region than those in the pockets, also indicating that the structures of the transition states can be effectively stabilized by the zeolite framework. Similarly, Wang and co-workers investigated the polyMB cycle in SAPO-34 with a similar cage structure and also observed a relatively low energy barrier for the formation of the spiro intermediate (SP1, 145 kJ mol^{-1}).[61] Moreover, the lower free energy barriers and higher rate constants of the propene elimination steps in the supercages also suggest that it is viable to decompose 1,1,2,6-tetramethyl-4-isopropylbenzenium cation, which is able to regenerate the active sites readily and then is beneficial in alleviating the rapid catalyst deactivation due to the carbonaceous deposition.

It should be noted that the free energy barriers for most steps via the polyMB cycle in the supercages are lower than those in the pockets, except those for the M1 and D2 steps. For the polyMB cycle in the pockets, as shown in Figure S1 of the Supporting Information, the transition states of M1 and D2 are obviously inserted into the pockets, in comparison with those of other steps. This means that the pockets and supercages have similar framework effects on the M1 and D2 steps; as a result, the free energy barriers for M1 and D2 in the pockets (139 and 83 kJ mol^{-1}, respectively) are also close to those in the supercages (144 and 94 kJ mol^{-1}, respectively). However, as the free energy barriers of the rate-determining steps (SP1 and HS1) via the polyMB cycle in the pockets are much higher than those in the supercages, the pockets in H-MCM-22 should play a minor role in MTO in comparison with the supercages.

The formation of the spiro intermediate (SP1) in the pockets and the supercages here is assisted by a water molecule; water as a proton transfer reagent may decrease the repulsive interaction between organic species and the zeolite framework and then facilitate the access of reacting species to the active sites.[11,55,61] On the other hand, fixing a water molecule in the transition state may also increase the activation entropy. As illustrated in Table S6 of the Supporting Information, the free energy barriers of SP1 without water assistance are about 19−33 kJ mol^{-1} lower than those with water assistance; however, the free energy changes between the reactant and product without water assistance are also elevated by 23−27 kJ mol^{-1} and the free energy barriers of the reverse reaction of SP1 are decreased by 42−60 kJ mol^{-1}. These suggest that the reverse reaction of SP1 is much easier in the case without water assistance, which may decrease the opportunities for the formation of the spiro intermediates and then has an adverse effect on the subsequent C−C bond breakage (SP2) to form propene. Moreover, because water is always present as a MTO byproduct in the reaction stream, it is groundless to exclude water from the polyMB cycle. Although water is generally considered being propitious to MTO, the detailed effects of water on the overall MTO process over different zeolites are worthy of an in-depth investigation in future works.

3.2.2. Alkene Cycle. Similar to those in the pockets, both C_6^+ and C_7^+ routes are considered for MTO over H-MCM-22 via the alkene cycle in the supercages (Figure 8). The calculated free energy profiles of the C_6^+ and C_7^+ routes in the supercages are shown in Figures 9 and 10, respectively; the free energy barriers and relative rate constants of each step in the alkene cycle are also given in Table 1. The framework of the supercages and the methanol and propene molecules in the gaseous phase are taken as the reference state to get the energies of other species. The calculated adsorption free energies of methanol and propene are 12 and 45 kJ mol^{-1}, respectively. The optimized transition states for the methylation step (M1) via the alkene cycle in the supercages are shown in Figure 11c, while other optimized transition states are presented in Figures S5a−e and S6a−g in the Supporting Information.

Via the C_6^+ route, the three methylation steps M1, M2(a), and M3(a) have free energy barriers of 150, 131, and 138 kJ mol^{-1}, with rate constants of 3.25×10^1, 9.44×10^2, and 2.62×10^2 s^{-1}, respectively. The two deprotonation steps of D1(a) and D2(a) are also very facile, with a free energy barrier below 45 kJ mol^{-1}. Propene is produced through the cracking of the C_6^+ ion; the free energy barrier and rate constant of this step (E1(a)) are 94 kJ mol^{-1} and 6.93×10^5 s^{-1}, respectively.

Via the C_7^+ route, the four methylation steps of M1, M2(b), M3(b), and M4(b) need to overcome free energy barriers of 150, 146, 134, and 141 kJ mol^{-1}, with rate constants of 3.25×10^1, 6.02×10^1, 5.55×10^2, and 1.69×10^2 s^{-1}, respectively. The three deprotonation steps of D1(b), D2(b), and D3(b) take place very easily, with free energy barriers below 45 kJ mol^{-1}. Propene is then generated through the cracking of the C_7^+ ion (E1(b)), which requires a free energy barrier of 88 kJ mol^{-1} with a rate constant of 1.91×10^6 s^{-1}.

The highest free energy barrier observed for MTO via the alkene cycle in the supercages is 150 kJ mol^{-1} for the M1 step, which is adjacent to the free energy barriers of M2(a) (149 kJ mol^{-1}) and M4(b) (143 kJ mol^{-1}) steps via the alkene cycle in the pockets. Table 2 also illustrates that the M1 step in the supercages and the M2(a) and M4(b) steps in the pockets are also quite similar in their enthalpy barrier and entropy loss. Figure 11c further depicts that the transition state for M1 via the alkene cycle in the supercages is wrapped in the internals of the supercages, which is stabilized by the zeolite framework. A large green region appears in the isosurface of M1, as shown in Figure 12c, indicating that the framework of the supercages can provide a transition state with pronounced electronic stabilization effects. Similarly, Chu and co-workers investigated the olefin reactions in mordenite zeolite with different pore structures and also found that an appropriate pore structure was vital to lower the activation energy of a reaction.[71]

The above results demonstrated that, for MTO in the supercages of H-MCM-22, propene can be effectively produced via the polyMB cycle; as the rate-determining step, the propene elimination reaction can readily occur through both the internal hydrogen-shift route (HS1, $\Delta G_{int}^{\ddagger}$ = 162 kJ mol^{-1}) and the spiro route (SP1, $\Delta G_{int}^{\ddagger}$ = 163 kJ mol^{-1}). Moreover, the alkene cycle also provides a viable pathway to the formation of propene, because both the methylation and cracking steps in the alkene cycle are also feasible; the highest free energy barrier observed in the alkene cycle is 150 kJ mol^{-1} for the methylation (M1). As a result, the supercages present in H-MCM-22 play a very important role in catalyzing the MTO reactions; propene is readily produced simultaneously via both the polyMB and alkene cycles. These results are supported by experimental studies on large cavity zeolite catalyzed MTO reactions by Bjørgen and co-workers.[72] Through cofeeding ^{13}C methanol with ^{12}C benzene, they found that higher polyMBs can be readily generated via simple methylations in the large cages of H-MCM-22 and serve as important intermediates for the formation of light olefins, implying that the supercages were the active centers crucial for the MTO reactions.

3.3. MTO in the Sinusoidal Channels. Previous investigations suggested that MTO over H-ZSM-22 (TON, 4.6 × 5.7 Å) might mainly proceed through the alkene

DOI: 10.1021/cs501232r
ACS Catal. 2015, 5, 1131−1144

methylation−cracking route, where the polyMB route was suppressed due to the restriction of the transition state by the interior narrow space.[58,59] The sinusoidal channels (4.1 × 5.1 Å) of H-MCM-22 are even smaller than the pores of H-ZSM-22. The formation of polyMBs and long branched alkenes is then seriously confined in these small sinusoidal channels. Therefore, the catalytic role of the sinusoidal channels will be considered by using the alkene cycle of the C_6^+ route, as the interior space is insufficient for the transition states of the C_7^+ route to make the geometry optimization. The calculated free energy profile and the detailed free energy barriers and rate constants for MTO over H-MCM-22 via the alkene cycle in the sinusoidal channels are also presented in Figure 9 and Table 1. The framework of the sinusoidal channels and the methanol and propene molecules in the gaseous phase are taken as the reference state to give the energies of other species. The calculated adsorption free energies of methanol and propene are −26 and 44 kJ mol^{-1}, respectively. The detailed optimized transition states for the alkene cycle in the sinusoidal channels are depicted in Figure 11d and Figure S7a−f in the Supporting Information.

The free energy barriers of the three methylation steps of M1, M2(a), and M3(a) are 180, 163, and 175 kJ mol^{-1}, respectively, which are markedly higher than those in the supercages; the corresponding rate constants (2.44 × 10^{-1}, 3.04 × 10^{0}, and 3.45 × 10^{-1} s^{-1}, respectively) are also lower than those in the supercages. Two deprotonation steps of D1(a) and D2(a) are viable, as their free energy barriers are lower than 80 kJ mol^{-1}. The propene molecule can be formed through the cracking of the C_6^+ ion; this step (E1(a)) requires a free energy barrier of 177 kJ mol^{-1}, which is about 83 kJ mol^{-1} higher than that in the supercages, with a rate constant of 2.71 × 10^{-1} s^{-1}, which is about 6 orders lower than that in the supercages (6.93 × 10^{5} s^{-1}).

As depicted in Table 2, the enthalpy barrier of the rate-determining step for the alkene cycle in the sinusoidal channels (M1, 136 kJ mol^{-1}) is close to that in the supercages (M1, 128 kJ mol^{-1}), whereas the entropy loss of M1 (44 kJ mol^{-1}) in the sinusoidal channels is markedly higher than that in the supercages (22 kJ mol^{-1}). It is evident that the narrow space of the sinusoidal channels limits the activity of methylation and olefin cracking and leads to an increase of the entropy loss, which may counteract the stabilization effect of the zeolite framework on the transition states.[49] In comparison with those in the supercages, the entropy losses and total free energy barriers for the methylation and olefin-cracking steps in the sinusoidal channels are dramatically elevated. The isosurface plots of the reduced density gradient in Figure 12d displays that there is a noteworthy increase of the red region for the transition state in the sinusoidal channels, although its green region is as large as that in the supercages. This also suggests that the steric constraints imposed by the narrow space in the sinusoidal channels may bring on the pronounced repulsive interaction and thus reduce the stability of the transition states.

The cracking of the C_5^+ ion of smaller size was also considered in the sinusoidal channels in this work; however, the results indicate that the cracking step of C_5^+ ion also requires a high free energy barrier of 188 kJ mol^{-1}, with a low rate constant of 3.69 × 10^{-2} s^{-1}. All these strongly suggest that the formation of propene in the sinusoidal channels is more difficult, in comparison with that in the supercages. The experimental observations by Matias and co-workers on the *n*-heptane transformation over H-MCM-22 zeolite have also shown that the sinusoidal channels were less active due to the space constraints by this narrow pore system.[73]

Figures 5, 9, and 10 show that methanol may prefer being adsorbed first in the sinusoidal channels with a much lower adsorption free energy, next in the supercages, and last in the pockets. For the adsorption of propene, the sinusoidal channels and the supercages may have similar opportunities, whereas the adsorption of 1,2,4,6-tetramethylbenzene prefers the supercages. For all of these three species, the pockets display the highest adsorption free energy, as the framework of the pockets cannot provide appropriate electrostatic stabilization effects to stabilize the adsorbates and the reaction intermediates.

For MTO via the polyMB cycles, the apparent free energies of all transition states in the supercages are evidently lower than those in the pockets (Figure 5). Moreover, the lower apparent free energy barrier in the supercages is mainly contributed by the lower apparent enthalpy barrier in the supercages (Table S7 in the Supporting Information), owing to the appropriate electrostatic stabilization effect provided by the supercages. For MTO via the alkene cycle, however, the apparent free energies of all the transition states in three types of pores are quite close (Figure 5), whereas the sinusoidal channels display a higher apparent free energy barrier for the methylation of propene (Table S7 in the Supported Information). The higher apparent free energy barrier in the sinusoidal channels is mainly attributed to the apparent entropy loss due to the steric constraints imposed by the narrow channels, which may lead to the pronounced repulsive interaction and thus reduce the stability of the transition states. Evidently, the apparent kinetics also give the same conclusions drawn on the basis of the intrinsic energy barriers: the difference of various pores in H-MCM-22 in their catalytic action on MTO is mainly attributed to their different framework structures; propene can be effectively produced in the supercages through both the polyMB and alkene cycles.

It should be noted that there are two distinct mechanisms for methylation, i.e. the concerted and stepwise pathways; which is the dominant pathway for alkene or arene methylations is still disputed in the literature.[74−76] As the stepwise pathway demands less space and is more likely to prevail in small voids of zeolites, methylation based on the stepwise pathway has also been calculated and compared with that based on the concerted pathway in the narrow sinusoidal channels. For the stepwise mechanism, Van der Mynsbrugge and co-workers investigated the formation and reactivity of framework-bound methoxide species and found that the methoxide formation is the rate-determining step for the stepwise mechanism.[77] In this work, therefore, the generation of methoxide is considered and the results reveal that the free energy barrier for the methoxide formation is 172 kJ mol^{-1} in the sinusoidal channels, which is just slightly lower than that of the rate-determining step for the concerted mechanism (M1, 180 kJ mol^{-1}), indicating that the stepwise mechanism cannot markedly reduce the free energy barriers of methylations in the sinusoidal channels. Even though the free energy barriers for methylations are depressed by following the stepwise methylation mechanism, the role of the sinusoidal channels played in MTO cannot be altered, as the free energy barrier for the cracking step (E1(a)) in the sinusoidal channels (177 kJ mol^{-1}) is still much higher than those in the supercages (94 kJ mol^{-1}). As a result, the mechanism of methylation has not been investigated further in this work.

DOI: 10.1021/cs501232r
ACS Catal. 2015, 5, 1131−1144

3.4. Catalytic Role of Various Pores in MTO over H-MCM-22. The above results clearly illustrate that three types of pores, i.e. the supercages, pockets, and sinusoidal channels, in H-MCM-22 are also rather different in their catalytic action on MTO because of the large differences in the pore size and shape that determine the space confinement and electrostatic stabilization effects. Propene is predicted to be mainly produced in the supercages, because both the polyMB and the alkene cycles are viable with relatively low free energy barriers and high rate constants for the methylation, deprotonation, and elimination/cracking steps in the supercages. The supercages with large pore size without evident space restriction are able to accommodate large polyMBs and long branched alkenes, which can serve as the active cocatalysts in the formation of propene. The quite low entropy losses and small red region in the isosurface plots of the reduced density gradient also suggest that the space confinement has a minor effect on MTO in the supercages. Meanwhile, as shown in Figure 6b1,b2 and Figure 7b1,b2, the framework of the cages can stabilize the transition states through the electrostatic stabilization effect, decrease the enthalpy barriers of the rate-determining step, and finally reduce the total free energy barriers.[49,54,64,71] As the olefin products can be eliminated readily in the cage, the opportunity for the development of large intermediates into coke may be reduced. In addition, the olefin products can be easily released through the 10-membered-ring (4.0 × 5.5 Å) windows in H-MCM-22, which are larger than the 8-membered-ring (3.8 × 3.8 Å) windows in H-SAPO-34; this may explain the fact that H-MCM-22 exhibits higher catalytic stability than H-SAPO-34 in MTO.[38]

In the sinusoidal channels of H-MCM-22, propene can only be produced through the alkene cycle of the C_6^+ route due to the space confinement; moreover, the transition states inside the narrow channels are restricted for lack of enough space and the entropy losses are markedly increased. As a result, the overall free energy barriers for the methylation and cracking steps in the sinusoidal channels are much higher than those in the supercages. Therefore, the contribution of the sinusoidal channels to the formation of propene in catalyzing MTO is relatively minor. Such a conclusion may conflict with the results of Min and co-workers,[38] in which they found that the sinusoidal channels contribute more to the reaction than the supercages. In current work, the sinusoidal channels, supercages, and pockets in H-MCM-22 are modeled by large clusters and other factors such as the carbonaceous deposition and framework alteration are not considered; as a result, the results obtained are more suitable to the initial period of MTO over the fresh H-MCM-22 catalyst. With the increase of the time on steam, however, the catalytic roles of various pores in MTO may also be influenced by the gradual carbonaceous deposition and framework alteration. In the case of Min and co-workers, the catalytic behavior of H-MCM-22 was considered during the later period, in which the activity of the supercages may be decreased with the gradual accumulation of coke species.

In the pockets of H-MCM-22, the quite high free energy barriers and very low rate constants for the olefin elimination/cracking steps in the polyMB cycle are mainly ascribed to the insufficiency of the electrostatic stabilization effect from the zeolite framework on the transition states, as depicted in Figure 6a1,a2 and Figure 7a1,a2; as a result, the transition states in the pockets are less stable and the enthalpy barriers are also markedly higher than those in the supercages. On the other hand, in the pockets, propene should be mainly generated via the alkene cycle. As a whole, however, the pockets may also be catalytically detrimental to the MTO process, as observed by Min and co-workers;[38] as the large 1,1,2,6-tetramethyl-4-isopropylbenzenium cation is facile to form but hard to decompose in the pockets, it may cover the active sites and even turn into coke, leading to the quick catalyst deactivation.

The difference of various pores of H-MCM-22 in their catalytic action in MTO should be ascribed to the difference in their framework structure and pore size, rather than to the variance in the acidic strength, although the acid strength of zeolites is in general an important factor influencing their catalytic performance.[78−81] The acid strength of the supercages, sinusoidal channels, and pockets was evaluated by the proton affinity (PA) of the active sites and ammonia adsorption energy (ΔE_{ads}) in these sites, as given in Table 3. The acid strength decreases in the order sinusoidal channels > supercages ≈ pockets. Evidently, the supercages and pockets exhibit similar acid strengths but rather different catalytic actions on MTO. Strong acidity is generally considered propitious to the cracking reaction;[82] however, current results indicate that the free energy barrier for the cracking of the C_6^+ ion is higher in the sinusoidal channels with stronger acidity in comparison to that in the supercages with weaker acidity. As a result, the acid strength of the active sites in different types of pores has an insignificant effect on their catalytic roles in MTO over the H-MCM-22 zeolite. These observations show that the zeolite framework is crucial to the MTO reactions, consistent with our previous investigations,[11] in which olefin eliminations over four kinds of zeolites with different pore sizes and shapes were comparatively investigated. The framework of a zeolite has a prominent influence on the energy barriers and the potential energy surface height and can then determine the detailed pathways of olefin formation in MTO.

Table 3. Calculated Proton Affinity (PA) and Ammonia Adsorption Energy (ΔE_{ads}) of the Active Sites in Supercages, Pockets, and Sinusoidal Channels of H-MCM-22 Zeolite

pore type	PA (kJ mol^{-1})	ΔE_{ads} (kJ mol^{-1})
supercage	1216	−128
pocket	1203	−122
sinusoidal channel	1160	−144

4. CONCLUSIONS

Three different types of pores, including the sinusoidal channels, supercages, and pockets in the H-MCM-22 zeolite, were depicted by large cluster models; their catalytic roles in the MTO process were investigated by DFT-D calculations.

The results demonstrated that the three types of pores are quite different in their catalytic action on MTO because of the large difference in the pore size and shape that determine the extent of space confinement and electrostatic stabilization effects. The formation of propene is mainly sustained in the supercages, where propene can be effectively produced through both the polyMB and the alkene cycles, as the supercage structure is appropriate to give the rate-determining steps a relatively low free energy barrier. In the sinusoidal channels, the free energy barrier of methylation and cracking steps is elevated due to the space confinement and the activity of alkenes is also markedly depressed in the narrow channels, in comparison with those in the supercages; as a result, the contribution of the

DOI: 10.1021/cs501232r
ACS Catal. 2015, 5, 1131−1144

sinusoidal channels to the whole propene formation is relatively minor. Meanwhile, the pockets are probably detrimental to MTO, as the facile formation of large intermediates such as 1,1,2,6-tetramethyl-4-isopropylbenzenium cation, which are difficult to decompose in the pockets due to the lack of electrostatic stabilization effect from the zeolite framework, may lead to a rapid deactivation of these active sites.

The calculated proton affinity and ammonia adsorption energy suggest that the acid strength of the active sites has little effect on the catalytic behaviors of various pores in H-MCM-22 and the zeolite framework structure is crucial to the MTO reactions; the evident variance of the supercages, sinusoidal channels, and pockets in their catalytic roles in MTO should be ascribed to the difference in the their pore sizes and structures.

■ ASSOCIATED CONTENT

Supporting Information

The following file is available free of charge on the ACS Publications website at DOI: 10.1021/cs501232r.

Comparison of the 6-31G(d) basis set with 6-31G(d,p), contribution of the van der Waals interaction to the total free energy barriers, the effect of intramolecular hydride shifts on the reaction pathways, the calculated free energy barriers and free energy changes of the spiro intermediate formation (SP1) with and without water assistance, the apparent energy barriers for the methylation of TMB and propene, and the detailed optimized transition states of various steps via the polyMB cycle and/or the alkene cycle in the pockets, supercages, and sinusoidal channels (PDF)

■ AUTHOR INFORMATION

Corresponding Authors

*Z.Q.: tel, +86-351-4046092; fax, +86-351-4041153; e-mail, qzhf@sxicc.ac.cn.

*J.W.: e-mail, iccjgw@sxicc.ac.cn.

Notes

The authors declare no competing financial interest.

■ ACKNOWLEDGMENTS

The calculations were performed on the Computer Network Information Center of the Chinese Academy of Sciences, National Supercomputer Centers in Shenzhen and Shanghai. The authors are grateful for the financial support of the National Basic Research Program of China (2011CB201400), the National Natural Science Foundation of China (21273264, 21273263, 21103216), and the Natural Science Foundation of Shanxi Province of China (2012011005-2, 2013021007-3).

■ REFERENCES

(1) Hickman, D. A.; Schmidt, L. D. *Science* **1993**, *259*, 343−346.
(2) Laurendeau, N. M. *Energy Combust. Sci.* **1978**, *4*, 221−270.
(3) Wen, W. Y. *Catal. Rev. Sci. Eng.* **1980**, *22*, 1−28.
(4) Asadullah, M.; Ito, S.; Kunimori, K.; Yamada, M.; Tomishige, K. *J. Catal.* **2002**, *208*, 255−259.
(5) Sutton, D.; Kelleher, B.; Ross, J. R. H. *Fuel Process. Technol.* **2001**, *73*, 155−173.
(6) Dahl, I. M.; Kolboe, S. *Catal. Lett.* **1993**, *20*, 329−336.
(7) Dahl, I. M.; Kolboe, S. *J. Catal.* **1994**, *149*, 458−464.
(8) Dahl, I. M.; Kolboe, S. *J. Catal.* **1996**, *161*, 304−309.
(9) Kolboe, S. *Acta Chem. Scand.* **1986**, *40*, 711−713.
(10) Wang, M.; Buchholz, A.; Seiler, M.; Hunger, M. *J. Am. Chem. Soc.* **2003**, *125*, 15260−15267.
(11) Wang, S.; Chen, Y. Y.; Wei, Z. H.; Qin, Z. F.; Chen, J. L.; Ma, H.; Dong, M.; Li, J. F.; Fan, W. B.; Wang, J. G. *J. Phys. Chem. A* **2014**, *118*, 8901−8910.
(12) Wei, Z. H.; Chen, Y. Y.; Wang, S.; Li, J. F.; Dong, M.; Qin, Z. F.; Wang, J. G.; Fan, W. B. *J. Fuel Chem. Technol.* **2013**, *41*, 897−910.
(13) Lesthaeghe, D.; Van Speybroeck, V.; Marin, G. B.; Waroquier, M. *Angew. Chem., Int. Ed.* **2006**, *45*, 1714−1719.
(14) Lesthaeghe, D.; Van Speybroeck, V.; Marin, G. B.; Waroquier, M. *Chem. Phys. Lett.* **2006**, *417*, 309−315.
(15) Song, W. G.; Haw, J. F.; Nicholas, J. B.; Heneghan, C. S. *J. Am. Chem. Soc.* **2000**, *122*, 10726−10727.
(16) Mikkelsen, O.; Ronning, P. O.; Kolboe, S. *Microporous Mesoporous Mater.* **2000**, *40*, 95−113.
(17) Mole, T.; Bett, G.; Seddon, D. *J. Catal.* **1983**, *84*, 435−445.
(18) Mole, T.; Whiteside, J. A.; Seddon, D. *J. Catal.* **1983**, *82*, 261−266.
(19) Sassi, A.; Wildman, M. A.; Ahn, H. J.; Prasad, P.; Nicholas, J. B.; Haw, J. F. *J. Phys. Chem. B* **2002**, *106*, 2294−2303.
(20) Song, W. G.; Nicholas, J. B.; Sassi, A.; Haw, J. F. *Catal. Lett.* **2002**, *81*, 49−53.
(21) Sullivan, R. F.; Sieg, R. P.; Langlois, G. E.; Egan, C. J. *J. Am. Chem. Soc.* **1961**, *83*, 1156−1160.
(22) Xu, T.; Haw, J. F. *J. Am. Chem. Soc.* **1994**, *116*, 7753−7759.
(23) Wang, C. M.; Wang, Y. D.; Liu, H. X.; Xie, Z. K.; Liu, Z. P. *Microporous Mesoporous Mater.* **2012**, *158*, 264−271.
(24) Dessau, R. M. *J. Catal.* **1986**, *99*, 111−116.
(25) Svelle, S.; Olsbye, U.; Joensen, F.; Bjørgen, M. *J. Phys. Chem. C* **2007**, *111*, 17981−17984.
(26) Bjørgen, M.; Svelle, S.; Joensen, F.; Nerlov, J.; Kolboe, S.; Bonino, F.; Palumbo, L.; Bordiga, S.; Olsbye, U. *J. Catal.* **2007**, *249*, 195−207.
(27) Lesthaeghe, D.; Van der Mynsbrugge, J.; Vandichel, M.; Waroquier, M.; Van Speybroeck, V. *ChemCatChem.* **2011**, *3*, 208−212.
(28) Wang, C. M.; Wang, Y. D.; Xie, Z. K. *J. Catal.* **2013**, *301*, 8−19.
(29) Stöcker, M. *Microporous Mesoporous Mater.* **1999**, *29*, 3−48.
(30) Djieugoue, M. A.; Prakash, A. M.; Kevan, L. *J. Phys. Chem. B* **2000**, *104*, 6452−6461.
(31) Lee, J. H.; Park, M. B.; Lee, J. K.; Min, H. K.; Song, M. K.; Hong, S. B. *J. Am. Chem. Soc.* **2010**, *132*, 12971−12982.
(32) Dai, W.; Wang, X.; Wu, G.; Guan, N.; Hunger, M.; Li, L. D. *ACS Catal.* **2011**, *1*, 292−299.
(33) Leonowicz, M. E.; Lawton, J. A.; Lawton, S. L.; Rubin, M. K. *Science* **1994**, *264*, 1910−1913.
(34) Shang, Y.; Yang, P. P.; Jia, M. J.; Zhang, W. X.; Wu, T. H. *Catal. Commun.* **2008**, *9*, 907−912.
(35) Corma, A.; Corell, C.; Flopis, F.; Martínez, A.; Pérez-Pariente, J. *Appl. Catal., A* **1994**, *115*, 121−134.
(36) Wu, P.; Komatsu, T.; Yashima, T. *Microporous Mesoporous Mater.* **1998**, *22*, 343−356.
(37) Zhu, Z. R.; Chen, Q. L.; Zhu, W.; Kong, D. J.; Li, C. *Catal. Today* **2004**, *93*, 321−325.
(38) Min, H. K.; Park, M. B.; Hong, S. B. *J. Catal.* **2010**, *271*, 186−194.
(39) Laforge, S.; Martin, D.; Guisnet, M. *Microporous Mesoporous Mater.* **2004**, *67*, 235−244.
(40) Rigoreau, J.; Laforge, S.; Gnep, N. S.; Guisnet, M. *J. Catal.* **2005**, *236*, 45−54.
(41) Meriaudeau, P.; Tuan, V. A.; Nghiem, V. T.; Lefevbre, F.; Ha, V. T. *J. Catal.* **1999**, *185*, 378−385.
(42) Camblor, M. A.; Corma, A.; Diaz-Cabanas, M. J.; Baerlocher, C. *J. Phys. Chem. B* **1998**, *102*, 44−51.
(43) Zhou, D. H.; Bao, Y.; Yang, M. M.; He, N.; Yang, G. *J. Mol. Catal. A* **2006**, *244*, 11−19.
(44) Zheng, A. M.; Lei, C.; Yang, J.; Zhang, M. J.; Su, Y. C.; Y, Y.; Y, C. H.; Deng, F. *J. Phys. Chem. B* **2005**, *109*, 24273−24279.
(45) Nguyen, C. M.; De Moor, B. A.; Reyniers, M. F.; Marin, G. B. *J. Phys. Chem. C* **2012**, *116*, 18236−18249.
(46) Liu, J. W.; Liu, Z. F.; Feng, G.; Kong, D. J. *J. Phys. Chem. C* **2014**, *118*, 18496−18504.

DOI: 10.1021/cs501232r
ACS Catal. 2015, 5, 1131−1144

(47) Maihom, T.; Pantu, P.; Tachakritikul, C.; Probst, M.; Limtrakul, J. *J. Phys. Chem. C* **2010**, *114*, 7850−7856.
(48) Boekfa, B.; Pantu, P.; Probst, M.; Limtrakul, J. *J. Phys. Chem. C* **2010**, *114*, 15061−15067.
(49) Van der Mynsbrugge, J.; De Ridder, J.; Hemelsoet, K.; Waroquier, M.; Van Speybroeck, V. *Chem.—Eur. J.* **2013**, *19*, 11568−11576.
(50) Van Speybroeck, V.; Van der Mynsbrugge, J.; Vandichel, M.; Hemelsoet, K.; Lesthaeghe, D.; Ghysels, A.; Marin, G. B.; Waroquier, M. *J. Am. Chem. Soc.* **2011**, *133*, 888−899.
(51) Frisch, M. J.; Trucks, G. W.; Schlegel, H. B.; Scuseria, G. E.; Robb, M. A.; Cheeseman, J. R.; Scalmani, G.; Barone, V.; Mennucci, B.; Petersson, G. A.; Nakatsuji, H.; Caricato, M.; Li, X.; Hratchian, H. P.; Izmaylov, A. F.; Bloino, J.; Zheng, G.; Sonnenberg, J. L.; Hada, M.; Ehara, M.; Toyota, K.; Fukuda, R.; Hasegawa, J.; Ishida, M.; Nakajima, T.; Honda, Y.; Kitao, O.; Nakai, H.; Vreven, T.; Montgomery, J. A., Jr.; Peralta, J. E.; Ogliaro, F.; Bearpark, M.; Heyd, J. J.; Brothers, E.; Kudin, K. N.; Staroverov, V. N.; Kobayashi, R.; Normand, J.; Raghavachari, K.; Rendell, A.; Burant, J. C.; Iyengar, S. S.; Tomasi, J.; Cossi, M.; Rega, N.; Millam, N. J.; Klene, M.; Knox, J. E.; Cross, J. B.; Bakken, V.; Adamo, C.; Jaramillo, J.; Gomperts, R.; Stratmann, R. E.; Yazyev, O.; Austin, A. J.; Cammi, R.; Pomelli, C.; Ochterski, J. W.; Martin, R. L.; Morokuma, K.; Zakrzewski, V. G.; Voth, G. A.; Salvador, P.; Dannenberg, J. J.; Dapprich, S.; Daniels, A. D.; Farkas, O.; Foresman, J. B.; Ortiz, J. V.; Cioslowski, J.; Fox, D. J. *Gaussian 09, revision A.02*; Gaussian, Inc., Wallingford, CT, 2009.
(52) Chai, J. D.; Head-Gordon, M. *Phys. Chem. Chem. Phys.* **2008**, *10*, 6615−6620.
(53) Goerigk, L.; Grimme, S. *Phys. Chem. Chem. Phys.* **2011**, *13*, 6670−6688.
(54) Van der Mynsbrugge, J.; Visur, M.; Olsbye, U.; Beato, P.; Bjørgen, M.; Van Speybroeck, V.; Svelle, S. *J. Catal.* **2012**, *292*, 201−212.
(55) De Wispelaere, K.; Hemelsoet, K.; Waroquier, M.; Van Speybroeck, V. *J. Catal.* **2013**, *305*, 76−80.
(56) Eyring, H. *J. Chem. Phys.* **1935**, *3*, 107−115.
(57) Lu, T.; Chen, F. W. *J. Comput. Chem.* **2012**, *33*, 580−592.
(58) Li, J. Z.; Wei, Y. X.; Qi, Y.; Tian, P.; Li, B.; He, Y. L.; Chan, F. X.; Sun, X. D.; Liu, Z. M. *Catal. Today* **2011**, *164*, 288−292.
(59) Li, J. Z.; Wei, Y. X.; Liu, G. Y.; Qi, Y.; Tian, P.; Li, B.; He, Y. L.; Liu, Z. M. *Catal. Today* **2011**, *171*, 221−228.
(60) Buchanan, J. S.; Santiesteban, J. G.; Haag, W. O. *J. Catal.* **1996**, *158*, 279−287.
(61) Wang, C. M.; Wang, Y. D.; Xie, Z. K.; Liu, Z. P. *J. Phys. Chem. C* **2009**, *113*, 4584−4591.
(62) Lesthaeghe, D.; Horre, A.; Waroquier, M.; Marin, G. B.; Van Speybroeck, V. *Chem. Eur. J.* **2009**, *15*, 10803−10808.
(63) Wang, C. M.; Wang, Y. D.; Liu, H. X.; Xie, Z. K.; Liu, Z. P. *J. Catal.* **2010**, *271*, 386−391.
(64) Lesthaeghe, D.; Van Speybroeck, V.; Waroquier, M. *Phys. Chem. Chem. Phys.* **2009**, *11*, 5222−5226.
(65) Johnson, E. R.; Keinan, S.; Mori-Sanchez, P.; Contreras-Garcia, J.; Cohen, A.; Yang, W. T. *J. Am. Chem. Soc.* **2010**, *132*, 6498−6506.
(66) Wang, C.; Chu, Y. Y.; Zheng, A. M.; Xu, J.; Wang, Q.; Gao, P.; Qi, G. D.; Gong, Y. J.; Deng, F. *Chem. Eur. J.* **2014**, *20*, 1−13.
(67) Zheng, A. M.; Liu, S. B.; Deng, F. *Microporous Mesoporous Mater.* **2009**, *121*, 158−165.
(68) Buchanan, J. *Appl. Catal.* **1991**, *74*, 83−94.
(69) Corma, A.; Orchilles, A. *Microporous Mesoporous Mater.* **2000**, *35*, 21−30.
(70) Mazar, M. N.; Al-Hashimi, S.; Cococcioni, M.; Bhan, A. *J. Phys. Chem. C* **2013**, *117*, 23609−23620.
(71) Chu, Y. Y.; Han, B.; Zheng, A. M.; Yi, X. F.; Deng, F. *J. Phys. Chem. C* **2013**, *117*, 2194−2202.
(72) Bjørgen, M.; Akyalcin, S.; Olsbye, U.; Benard, S.; Kolboe, S.; Svelle, S. *J. Catal.* **2010**, *275*, 170−180.
(73) Matias, P.; Lopes, J. M.; Laforge, S.; Magnoux, P.; Guisnet, M.; Ramoa Ribeiro, F. *Appl. Catal., A* **2008**, *351*, 174−183.
(74) Ilias, S.; Bhan, A. *ACS Catal.* **2013**, *3*, 18−31.
(75) Brogaard, R. Y.; Henry, R.; Schuurman, Y.; Medford, A. J.; Mosed, P. G.; Beato, P.; Svelle, S.; Norskov, J. K.; Olsbye, U. *J. Catal.* **2014**, *314*, 159−169.
(76) Gomes, J.; Head-Gordon, M.; Bell, A. T. *J. Phys. Chem. C* **2014**, *118*, 21409−21419.
(77) Van der Mynsbrugge, J.; Moors, S. L. C.; De Wispelaere, K.; Van Speybroeck, V. *ChemCatChem* **2014**, *6*, 1906−1918.
(78) Wang, Y.; Yang, G.; Zhou, D. H.; Bao, X. H. *J. Phys. Chem. B* **2004**, *108*, 18228−18233.
(79) Chu, Y. Y.; Han, B.; Zheng, A. M.; Deng, F. *J. Phys. Chem. C* **2012**, *116*, 12687−12695.
(80) Erichsen, M. W.; Svelle, S.; Olsbye, U. *J. Catal.* **2013**, *298*, 94−101.
(81) Erichsen, M. W.; Svelle, S.; Olsbye, U. *Catal. Today* **2013**, *215*, 216−223.
(82) Zhu, X. X.; Liu, S. L.; Song, Y. Q.; Xu, L. Y. *Appl. Catal., A* **2005**, *288*, 134−142.

DOI: 10.1021/cs501232r
ACS Catal. 2015, 5, 1131−1144